



**HAL**  
open science

## **FIB plan view lift-out sample preparation for TEM characterization of periodic nanostructures obtained by spinodal decomposition in Co<sub>1.7</sub>Fe<sub>1.3</sub>O<sub>4</sub> thin films**

Thi Ty Mai Dinh, Antoine Barnabé, Thi Mai Anh Bui, Claudie Josse, Teresa Hungría, Corine Bonningue, Lionel Presmanes, Philippe Tailhades

### ► To cite this version:

Thi Ty Mai Dinh, Antoine Barnabé, Thi Mai Anh Bui, Claudie Josse, Teresa Hungría, et al.. FIB plan view lift-out sample preparation for TEM characterization of periodic nanostructures obtained by spinodal decomposition in Co<sub>1.7</sub>Fe<sub>1.3</sub>O<sub>4</sub> thin films. CrystEngComm, 2018, 20 (40), pp.6146-6155. 10.1039/C8CE01186A . hal-02321671

**HAL Id: hal-02321671**

**<https://hal.science/hal-02321671>**

Submitted on 21 Oct 2019

**HAL** is a multi-disciplinary open access archive for the deposit and dissemination of scientific research documents, whether they are published or not. The documents may come from teaching and research institutions in France or abroad, or from public or private research centers.

L'archive ouverte pluridisciplinaire **HAL**, est destinée au dépôt et à la diffusion de documents scientifiques de niveau recherche, publiés ou non, émanant des établissements d'enseignement et de recherche français ou étrangers, des laboratoires publics ou privés.



## Open Archive Toulouse Archive Ouverte (OATAO)

OATAO is an open access repository that collects the work of Toulouse researchers and makes it freely available over the web where possible

This is an author's version published in: <http://oatao.univ-toulouse.fr/24537>

**Official URL:** <https://doi.org/10.1039/C8CE01186A>

### To cite this version:

Dinh, Thi Ty Mai  and Barnabé, Antoine  and Bui, Thi Mai Anh  and Josse, Claudie and Hungria, Teresa and Bonningue, Corine  and Presmanes, Lionel  and Tailhades, Philippe  *FIB plan view lift-out sample preparation for TEM characterization of periodic nanostructures obtained by spinodal decomposition in Co<sub>1.7</sub>Fe<sub>1.3</sub>O<sub>4</sub> thin films.* (2018) CrystEngComm, 20 (40). 6146-6155. ISSN 1466-8033

Any correspondence concerning this service should be sent to the repository administrator: [tech-oatao@listes-diff.inp-toulouse.fr](mailto:tech-oatao@listes-diff.inp-toulouse.fr)

# FIB plan view lift-out sample preparation for TEM characterization of periodic nanostructures obtained by spinodal decomposition in $\text{Co}_{1.7}\text{Fe}_{1.3}\text{O}_4$ thin films.

T.M.C. DINH<sup>a, b</sup>, A. BARNABE<sup>\*a, c</sup>, M.A. BUI<sup>a, d</sup>, C. JOSSE<sup>c</sup>, T. HUNGRIA<sup>c</sup>, C. BONNINGUE<sup>a</sup>, L. PRESMANES<sup>a</sup>, P. TAILHADES<sup>a</sup>

<sup>a</sup> CIRIMAT, Université de Toulouse, CNRS, UT3 – Paul Sabatier, 118 Route de Narbonne 31062 TOULOUSE Cedex 9 France.

<sup>b</sup> University of Science, Vietnam National University Ho Chi Minh City, 227 Nguyen Van Cu St., Ward 4, District 5, Ho Chi Minh City, Vietnam.

<sup>c</sup> Centre de Microcaractérisation Raimond CASTAING, Université de Toulouse, CNRS, UT3 – Paul Sabatier, INP, INSA, Espace Clément Ader, 3 rue Caroline Aigle, 31400 TOULOUSE France.

<sup>d</sup> University of Transport and Communications, No 3 Cau Giay St., Dong Da District, Hanoi 112345, Vietnam.

## Abstract

There is a miscibility gap in the  $\text{CoFe}_2\text{O}_4$ - $\text{Co}_3\text{O}_4$  phase diagram. In this miscibility gap, the oxides can be subjected to a spinodal transformation. It has already been observed in oxides consisting of crystals greater than or equal to 100 nm that the spinodal decomposition leads to the formation of two alternating iron-rich and cobalt-rich spinel phases. The pseudo-periodic alternation occurs approximately every 5 nm. In the miscibility gap, the thin films of pure iron cobaltites, consisting of crystallites of the order of 10 nm in diameter and of a thickness of around 300 nm, undergo a transformation when they are treated at 600 °C for several hours. X-ray diffraction and Raman spectroscopy clearly reveal this transformation, which is accentuated as a function of the treatment time. An electron microscopy study of cross-sections (view of the films along their thickness), confirms the progressive separation of the former spinel oxide in iron-rich and cobalt-rich spinel phases, without, however revealing a pseudo-periodic organization of these phases, whatever the time of treatment. In an attempt to reveal this organization, a specific method of preparation has been implemented to extract the upper part of the films parallel to their basic plane and to observe the crystallites in plan view. The alternation of the iron- and cobalt-rich phases could, however, only be found in the largest crystallites. It seems that the nanometric size of the crystallites prevents the establishment of a pseudo-periodic organization of the phases during the periodic transformation. The observation of compositional anomalies in grain boundaries seems to support this hypothesis related to a nanometric effect of the crystallization.

## 1. Introduction

The iron - cobaltites spinel  $\text{Co}_{3x}\text{Fe}_{3-3x}\text{O}_4$  ( $x \geq 0.5$ ) have not so far been as widely used in the industry as other spinels such as ferrites in particular. Their properties, however, are of interest for certain technological applications, among which can be mentioned the electrodes for batteries and supercapacitors [1,2], the absorber layers in high-performance solar cells [3], the magnetic logic cells [4] and the microwave components [5]. The formation of periodic organizations at a nanoscale by spinodal decomposition within the miscibility gap of the  $\text{CoFe}_2\text{O}_4$ - $\text{Co}_3\text{O}_4$  phase diagram also makes it possible to imagine their use in magnetoresistance components. Indeed, giant magnetoresistance effects have already been demonstrated in alloys structured by spinodal decomposition [6, 7]. In a more prospective way, one could also hope to form structures having properties comparable to those of the magnonic crystals [8, 9].

The  $\text{CoFe}_2\text{O}_4$ - $\text{Co}_3\text{O}_4$  phase diagram has been established from experimental results [10, 11, 12] and also calculated from thermodynamic data [13, 14, 15]. An illustration of these calculated phase diagrams is given in Figure 1 in the  $0.3 \leq x \leq 1$  composition range whereas  $x = \text{Co}/(\text{Co}+\text{Fe})$ . It shows a miscibility gap below approximately 700 °C, which extends between about  $x = 0.37$  ( $\text{Co}_{1.1}\text{Fe}_{1.9}\text{O}_4$ ) and  $x = 0.90$  ( $\text{Co}_{2.7}\text{Fe}_{0.3}\text{O}_4$ ) at room temperature. Pure iron cobaltites obtained at around 900 °C in air are therefore subjected to a phase transformation during their cooling or during long-term heat

treatments at a temperature below 700 °C. This transformation initially occurs by spinodal decomposition. This process observed in miscibility gaps of many phase diagrams has been described by Cahn and Hilliard works [16, 17] on the one hand, and schematized and experimentally illustrated by Harrison and Putnis [18], on the other hand. For the Co-Fe-O system, it leads to the formation at the nanoscale, of pseudo-periodic alternations of cobalt rich and iron rich spinel phases in the central part of the spinel miscibility gap, i.e. in between  $x \approx 0.47$  ( $\text{Co}_{1.4}\text{Fe}_{1.6}\text{O}_4$ ) and  $x \approx 0.83$  ( $\text{Co}_{2.5}\text{Fe}_{0.5}\text{O}_4$ ) according to Takahashi et al. [12]. When the composition of the spinel phase exceeds these limits, i.e. for  $0.37 \leq x \leq 0.47$  in the iron rich part, and for  $0.83 \leq x \leq 0.90$  in the cobalt rich part, the spinodal decomposition is relayed by a germination growth mode. This mode allows the precipitation of two spinels of even more differentiated compositions respectively rich in cobalt ( $\text{Co}_{2.7}\text{Fe}_{0.3}\text{O}_4$ ) or rich in iron ( $\text{Co}_{1.1}\text{Fe}_{1.9}\text{O}_4$ ) and the grains of each phase are no longer distributed according to a periodic organization.

The alternations of cobalt rich and iron rich spinel phases due to spinodal decomposition in Co-Fe-O system have already been observed in well-crystallized thin films or powders initially synthesized at 900 °C and subsequently annealed at 700 °C [19, 20] or in films deposited under magnetic field on single crystal substrates by pulsed laser deposition [21]. In the recent studies, the  $\text{Co}_{1.75}\text{Fe}_{1.25}\text{O}_4$  thin films were directly prepared by radio-frequency sputtering [22]. Thanks to this method, which generates only very moderate temperature elevations, the nano-crystallized films have been obtained. Although the concomitant formation of iron cobaltite spinel and mixed cobalt iron monoxide tends to occur, the implementation of a low working pressure (0.5 Pa in argon pressure) for a magnetron sputtering power of  $1.3 \text{ W}\cdot\text{cm}^{-1}$ , made it possible to obtain films virtually free of monoxide. The spinodal decomposition of such cobaltite films was studied by X-ray diffraction analysis as well as by Raman spectroscopy [23]. The high sensitivity of this spectroscopic technique, allowed to characterize the very beginning of the spinodal decomposition and revealed that a heat treatment at 300 °C for 2 h is enough to start the decomposition.

The cross sections of  $\text{Co}_{1.7}\text{Fe}_{1.3}\text{O}_4$  films were already observed by Scanning Transmission Electron Microscopy (STEM) and analyzed by X-ray energy dispersive spectroscopy by the present authors [23]. A rather homogeneous distribution of iron and cobalt cations in samples annealed at 600 °C for 24 h could be demonstrated. A clear segregation of cobalt-rich phases, on the one hand, and iron-rich ones, on the other hand, was revealed in samples heated to the same temperature, but treated for 96 h. It was not possible, however, to find in the samples examined the pseudo-periodic alternations of spinel phases of different compositions, characteristic of the spinodal decomposition. The superimposition of crystallites of different orientations or compositions within the transverse sections studied, could be one of the reasons why the characteristic images of a spinodal decomposition could not be observed. The influence of the small size of the constitutive crystallites in the films on the mechanisms of the spinel phases separation could also be responsible for the absence of regular alternations of phases rich in cobalt and iron.

In this work, we try to extract the upper part of the layers parallel to the surface of the  $\text{Co}_{1.7}\text{Fe}_{1.3}\text{O}_4$  films which is made up of the largest and best-organized crystallites at the atomic scale. The objective was to have thin samples whereas, perpendicular to their plane, we could observe areas in which most of the crystallites would occupy the entire thickness. Indeed, this configuration avoids the different crystalline network superimposition which is disadvantageous for a high resolution observation of very good quality and to draw clear conclusion about spinodal mechanisms in nanocrystals. This work, therefore, raises the challenge of unconventional sample preparation by the Focussed Ion Beam (FIB) cutting technique. Also, it attempts to advance in the understanding of spinodal decomposition mechanisms in nano-crystalline thin films and to reveal a possible nanoscale effect on this phase transformation process.

## 2. Experimental

The  $\text{Co}_{1.7}\text{Fe}_{1.3}\text{O}_4$  spinel films were prepared by magnetron radio frequency (RF) sputtering using a homemade ceramic target (conditions of preparation of the target described in previous work [23]). The sputtering apparatus is an Alcatel A450 deposition system equipped with a radio frequency-generator (13.56 MHz) device, a pumping system, a gas flow controller, a water-cooled target holder and two water-cooled sample holders. The films were deposited at room temperature on water-cooled silicon substrates. A residual vacuum close to  $5 \times 10^{-5}$  Pa was reached in the sputtering chamber before introducing the argon deposition gas. At the beginning, the target was pre-sputtered for 20 hours to avoid any contamination. The target was also sputtered for 10 minutes before each film deposition. The sputtering conditions (20 W of RF power, 0.5 Pa in argon pressure and 5 cm in target to substrate distance) were optimized to obtain pure  $\text{Co}_{1.7}\text{Fe}_{1.3}\text{O}_4$  spinel films [23]. Deposition rates were first calculated from the deposition time and thickness of calibration films determined using a Dektak 3030ST mechanical profilometer. The thickness of the films was then fixed to 300 nm for all the studied samples in this work by adjusting the deposition time.

Ex-situ annealings were carried out in air at 600 °C for various time up to 96 h in order to promote the spinodal decomposition. The structural characterization of the films was performed at room temperature by Grazing Incidence angle X-Ray Diffraction (GIXRD) with  $\alpha = 1$  deg. on a Siemens D5000 diffractometer equipped with a Bruker Sol-X detector. The X-ray wavelength was that of the copper  $\text{K}\alpha$  rays ( $\text{K}\alpha_1 = 1.5405 \text{ \AA}$  and  $\text{K}\alpha_2 = 1.5443 \text{ \AA}$ ). Lattice constants were refined by the Rietveld method using the Full Prof-Win Plot R program [24, 25].

Raman spectra were collected under ambient conditions using a LabRAM HR 800 Jobin Yvon spectrometer with a laser excitation wavelength of 532 nm. Spectra acquisition was carried out for 200 sec using  $\times 100$  objective lens and 600 g/mm grating. During the measurement, the resulting laser power at the surface of the sample was adjusted to 0.7 mW to avoid the transformation of the ferrite thin film (especially to avoid spinodal decomposition). The examination of multiple spots showed that the samples were homogeneous.

The structure, microstructure and composition were investigated by Transmission Electron Microscopy (TEM) using a combination of high-resolution cross-sectional imaging in STEM and conventional TEM modes, Selected Area Electron Diffraction (SAED) and X-ray Energy Dispersive Spectroscopy (EDS). TEM studies were carried out using a JEOL JEM-ARM200F spherical-aberration probe corrected electron microscope equipped with a cold field emission gun operated at 200 kV, an ultrafast Ultrascan 2k x 2k camera (Gatan) for TEM, bright field (BF) and high-angle annular dark field (HAADF) detectors (JEOL) for STEM imaging, a Centurio X-ray detector (JEOL) for ultra-high resolution EDS mappings. To prepare cross sectional samples for TEM studies, slices from the sample were cut, placed between spacer layers and then glued onto a grid in such a way that the interface is parallel to the slot in the grid. This sample is then thinned by standard tripod polishing until it is a few  $\mu\text{m}$  thick. The final sample is thinned using a Gatan PIPS 691 ion beam miller to create an electron transparent sample. The method of preparing plan view sections by Focussed Ion Beam (FIB) was one of the focus of this work. This method is described in detail in the following section.

### 3. Results and discussion

#### 3.1. As-deposited sample

The structural analysis of the as-deposited and annealed samples at 600 °C under air has been detailed previously [23] by the present authors. As-deposited sample is made of small crystallites of about a few tens of nanometers, with an average composition  $x = 0.58$ . No extra phase could be detected by GIXRD measurements, as shown in Figure 2a. The cubic  $\text{Co}_{1.7}\text{Fe}_{1.3}\text{O}_4$  spinel phase was refined in the  $F\bar{4}3m$  ( $n^\circ 166$ ) space group and this leads to a lattice parameter close to  $a = 8.26 \text{ \AA}$ . The broadening of the diffraction peaks was in good agreement with the particle size determined by atomic force microscopy (not shown here) and TEM.

#### 3.2. Annealed samples and first characterisation of the spinodal decomposition

With the annealing time at 600 °C under air, a clear split of the most intense diffraction peaks (i.e. (311) and (440)) occurs. This split corresponds to the apparition of two spinel phases that evolve with more and more different lattice constants. The main diffraction peaks observed on the as-deposited film shift towards the higher diffraction angles during the first hours of annealing, as pointed out by the green arrow in Figure 2a and confirmed by the decreasing of the refined lattice parameter (Figure 2b). It corresponds to the progressive growth of the cobalt rich phase induced by the spinel miscibility gap. It is confirmed by the apparition of the iron rich counterpart phase characterized by a second set of diffraction peaks (red arrow) which 1) appears at lower angles and 2) shift towards the lower angles during the annealing process. Based on reference lattice parameters refined on eight homemade powders elaborated at 900 °C and quenched down to room temperature to obtain pure spinel phase in the  $0.33 \leq x \leq 1$  range (not shown here), the Vegard law allows to add on Figure 2b the limit of the miscibility gap (i.e.  $0.37 \leq x \leq 0.90$  according to thermodynamic calculations [13]) as well as the limit of the coherent spinodal domain (i.e.  $0.47 \leq x \leq 0.83$  according to Takahashi et al. [12]). One can note on Figure 2b that, for duration smaller than 24 h, the lattice parameters of both spinels phases obtained by spontaneous decomposition correspond to compositions within the coherent spinodal domain, i.e. with an expected pseudo-periodic alternation of cobalt rich and iron rich spinel phases. For duration greater than 24 h, the lattice parameters exceed these limits, and the spinodal decomposition is supposed to be relayed by a germination growth mode with a concomitant disappearance of the periodic organization at the nanoscale. The lattice parameters of the film annealed for 96 h tend to those of the powder samples at the limit of the miscibility gap proposed by Jung et al. [13], but not completely. This could be due to 1) the very slow kinetic of the decomposition process as demonstrated, for instance, by the very small changes of the cobalt-rich phase parameter (8.16 Å for 24h down to 8.15 Å for 96h) observed in Figure 2b, 2) an inaccuracy in the spinel miscibility gap limits, as many authors did not report exactly the same values (see for instance thermodynamic calculations [13, 14] plotted in Figure 1, or experimental data [10, 12]), or 3) limitations due to nanocrystalline and/or stress phenomena in thin film materials.

The spontaneous decomposition is also confirmed by the Raman spectroscopy, as shown in Figure 3a. The main peaks related to the spinel oxides and already identified in previous studies [26, 27, 28] are present and these main peaks evolve with the duration of the heat treatment. More specifically and using the terminology of Z. Wang et al. [29] and O.N. Shebanova et al. [30], these changes concern the very strong growth of the  $T_{2g}(1)$  and  $A_{1g}$  peaks at around 180 and 650  $\text{cm}^{-1}$ , respectively, and the emergence of low-intensity  $E_g$  and  $T_{2g}(2)$  peaks at around 290 and 450  $\text{cm}^{-1}$ , respectively. The Raman peak intensities after 96 h of annealing at 600 °C under air could be convolved with the ones of the  $x = 0.37$  and  $x = 0.90$  powder reference samples (Figure 3b), i.e. it converges to the complete decomposition of the pristine phase. For the intermediate annealing duration of 12 and 24 h, the Raman peak evolution is on-going and confirms the step of spinodal decomposition that is in good agreement with the previous XRD studies and previous works [23].

In the XRD and Raman studies, in addition to the pristine as-deposited film, two annealed samples were identified as key samples in the characterization of this spontaneous decomposition. The first one is the sample annealed for 24 h, because it was identified to be among those where the spinodal decomposition ends, i.e. it could be the most appropriate sample to highlight the pseudo-periodic alternations of cobalt rich and iron rich spinel phases. The second one is the sample annealed for 96 h, because it corresponds to the longest annealing time, i.e. the best sample to highlight the microstructure changes induced by the germination-growth mode change. To have samples observable by TEM, both annealed films were prepared according to the specific thinning process described above.

### 3.3. TEM studies

First TEM characterizations carried out on cross-section samples (already published by the present authors [23]) reveal that no clear contrast between the two phases formed by spinodal transformation at 600 °C for 24 h, could be highlighted. Local chemical

analyses were also unable to reveal distinct phases, as shown by the homogeneous distribution of the iron and cobalt species in the cross section STEM view.

However, the complete segregation, which occurs after a much longer annealing time (96 h) at 600 °C, displays cobalt rich and iron rich regions of about 50 nm in diameter, as shown in green and red areas, respectively, in Figure 4a. The random distribution of the two phases in these regions along and perpendicular to the columns reveals, however, that the spinodal transformation is replaced by a nucleation and growth process for such a very long time of treatment at 600 °C. Some iron-rich and cobalt rich areas could be highlighted (Figure 4c). Semi-quantitative determination of the chemical composition of the phases can be done by EDS in these areas. The compositions close to  $\text{Co}_{1.3}\text{Fe}_{1.7}\text{O}_4$  and  $\text{Co}_{2.1}\text{Fe}_{0.9}\text{O}_4$  have been obtained. They sensitively differ from the average  $\text{Co}_{1.7}\text{Fe}_{1.3}\text{O}_4$  composition of the as-deposited film. The local variations of iron and cobalt at the 50 nm scale (i.e. the column width) are also visible from the 300 nm linear analysis shown in Figure 4d, but cannot be exactly defined at lower scale (i.e. within the column diameter). This is due to the limited resolution of the apparatus, which implies to select small areas of few tens of  $\text{nm}^2$  at minimum, for EDS quantification, but also to the superimposition of the columns in the thickness of the sample studied. The cross section coming from the standard thinning process, leads to thickness of few tens of nanometers, which is a little bit bigger than the diameter of the columns. Consequently, it's quite impossible to observe single crystalline domains, and then, even more to highlight nanoscale organisation induced by spinodal decomposition within the columns. In the STEM images (Figure 4b) and corresponding EDS mapping (Figure 4a), of the 600 °C - 96 h annealed sample, a homogeneous distribution of Co and Fe could be seen in more than a third of the total length of the columns, i.e. for 100 - 150 nm (see examples of Co-rich and Fe-rich areas drawn in Figure 4a and Figure 4b). As a result, a second set of samples, dedicated to TEM studies, were then cut from the upper part of the thin films, in a direction parallel to their plane. This very delicate preparation capable of revealing monocrystalline domains, has been implemented as follows.

The TEM specimens of 24 h and 96 h annealing time were then prepared using a FEI Helios Nanolab600i dual beam SEM FIB fitted with an Easylift micromanipulator for in situ lift-out. The ion column was operated at 30 kV for all steps, except for final cleaning of the specimen, for which tensions of 5 kV and 2 kV were used. Beam currents varied between 47 nA and 15 pA. Figure 5 shows the main stages in the production of plan-view TEM specimens of thin films (300nm). The sample was first mounted horizontally in the chamber and a region located at the edge of the thin film was chosen for the future observation (Figure 5a). The reason for choosing an area at the edge of the film was that the edge could be used as the top surface for the final prepared sample and that it could be easily grasped and removed. The electron beam was used to deposit a layer of Pt 200 nm thick over an area of 30  $\mu\text{m}$  wide and 15  $\mu\text{m}$  tall. The ion beam was then used to deposit a 3  $\mu\text{m}$  thick layer over the same area (Figure 5b). A preliminary regular cross section pattern was defined so that it overlaps with the bottom edge of the Pt strip. Then, a cleaning cross section was milled (Figure 5c). Next, the sample was removed from the chamber and re-mounted vertically with the edge of the film that was identified in the previous step now topmost (Figure 5d). The same area that was coated previously, was located and a 20  $\mu\text{m}$  x 2  $\mu\text{m}$  layer of ion beam 3  $\mu\text{m}$  thick platinum was deposited on top (Figure 5e). The preparation could now proceed in a similar fashion to standard TEM specimen preparation, except material only had to be removed from one side of the specimen. This was done using a standard cross-section milling pattern, to reach a final depth of around 15  $\mu\text{m}$  (Figure 5f). The specimen was then partially cut-out and a Pt needle was fixed (Figure 5g). The sample was lifted out in situ (Figure 5h) and then attached to a copper support grid (Figure 5i). Thinning of the specimen could then proceed using a gradual cross-section cleaning milling pattern, with a final milling beam current of 80 pA (Figure 5j). Finally, the 5 kV and 2 kV cleaning steps were carried out on each side (Figure 5k). The great care is topical in making specimens from thinner films so that the film was not lost during the thinning process.

First, the 96 h annealed film was analysed and compared to previous studies [23] and Figure 4. The TEM results are shown in Figure 6.

In the STEM image (Figure 6a), the previously observed columnar structure is evidenced by grains of around 20 nm in diameter, which correspond to the column section. The high resolution imaging in HAADF-STEM and BF-STEM modes (Figure 6d, and Figure

6e) confirms that most of the selected areas are single crystalline, i.e. that the thinning process was successful and allow to characterize the upper part of a single column. No specific crystallographic orientation could be found and this is in good agreement with the previous XRD studies and the cubic symmetry of the spinel structure.

The average  $\text{Co}_{1.8}\text{Fe}_{1.2}\text{O}_4$  composition deduced from the total spectrum (Figure 6a) is close to the nominal  $\text{Co}_{1.7}\text{Fe}_{1.3}\text{O}_4$ . The slight difference is due to the limited analysed area ( $1.3 \mu\text{m}^2$ ) and clear segregation of cobalt-rich phases, on the one hand, and iron-rich, on the other hand, which were evidenced by EDS mapping (Figure 6b and Figure 6c). The homogeneous Co-rich and Fe-rich compositions could be observed and they reach up the  $\text{Co}_{2.3}\text{Fe}_{0.7}\text{O}_4$  (Figure 6b) and  $\text{Co}_{1.2}\text{Fe}_{1.8}\text{O}_4$  (Figure 6c) compositions, respectively, in selected areas smaller than the columns diameter. These compositions correspond to the average ones recorded on twelve different selected areas.

The Fe-rich composition with a  $\text{Co}/(\text{Co}+\text{Fe})$  ratio of 0.4 is almost the one expected by the phase diagram (Figure 1). This ratio is below the one of the limit of the spinodal transition and could explain the relative homogeneity of the composition within the grain evidenced by atomic scale elemental analysis plotted in Figure 6g. This is also in good agreement with the XRD results (Figure 2).

Oppositely, the Co-rich composition only reach a  $\text{Co}/(\text{Co}+\text{Fe})$  ratio of 0.8, which corresponds to the limit of the spinodal and germination growth mode transition. During the first step of the decomposition process, the pristine spinel phase tends to form the Co-rich spinel phase, as shown by XRD. To compensate, the Fe-rich counterpart segregates to the grain boundary and, then, it forms the Fe-rich spinel phase in surrounding grains/columns. This increase in Fe content is evidenced on the right side of line scan 1 (Figure 6g) and on the central part of line scan 2 (Figure 6i).

The 24 h annealed film was then analysed in order to identify, within the column width, the specific atomic arrangement due to the spinodal decomposition process. The well-organized and single phase domains are predominantly present in the whole film as demonstrated by a  $[\bar{1}\bar{1}\bar{1}]$  zone axis oriented grain (HAADF-STEM image in Figure 7d and corresponding to Fast Fourier Transform (FFT) pattern in Figure 7e. Typical inter-planar distance of  $2.9 \text{ \AA}$  could be measured in good agreement with the  $d_{220}$  of cubic spinel with lattice constant close to  $a = 8.2 - 8.3 \text{ \AA}$ .

The average composition deduced from the total EDS spectrum over the limited area of  $0.01 \mu\text{m}^2$  was found to be  $\text{Co}_{1.8}\text{Fe}_{1.2}\text{O}_4$  (Figure 7a). This composition is close to the nominal one, as for the 96 h annealed sample.

The analyses carried out on very small selected area with typical size smaller than the column diameter allow determining the extreme Fe-rich and Co-rich areas. These areas are selected from the EDS mapping, as shown, for example, in Figure 7b and Figure 7c. The Fe-rich and Co-rich compositions reach up a  $\text{Co}/(\text{Co}+\text{Fe})$  ratio of 0.4 and 0.7, respectively. These limits (0.4 and 0.7) obtained after 24h of annealing treatment are similar or smaller than the ones (0.4 and 0.8) obtained after 96h. With the annealing time increase, the Co content evolves in the Co-rich part that is in good agreement with the XRD studies and consolidates the fact that the transition is still on going. Nevertheless, the Fe-rich composition is found to be outside the predicted limit of the spinodal transition domain, which supposes that the expected pseudo-periodic alternations of cobalt rich and iron rich spinel phases have disappeared. This is in good agreement with the fact that in each crystallized domain the composition is fairly homogeneous.

Further study, however, shows crystallites in which composition heterogeneities are observed for the sample treated at  $600 \text{ }^\circ\text{C}$  for 24 h. This case is encountered for crystallites with the largest sizes. Figure 7 illustrates this. If the chemical composition is homogeneous according to the small size of the crystallite (Figure 7f and Figure 7h), it is not the same in the direction of elongation (Figure 7f and Figure 7g). The upper part of the grain exhibits cobalt excess with a  $\text{Co}/(\text{Co}+\text{Fe})$  ratio close to 0.8 as the lower part exhibits iron excess with a Co ratio close to 0.4.

These results demonstrate that the sample treated for 24 h, for which it is expected to observe pseudo-periodic composition variations induced by the spinodal transformation, rarely shows this characteristic. From the previous observations, this sample is at the limit of the spinodal transformation and nucleation-growth domains. The infrequent occurrence of pseudo-periodic alternations of phases, respectively rich in iron and cobalt, could potentially result from the state of progress of the formation of the two spinel phases. However, the characteristic alternation of the phases is observed only when the crystallites have at least one

dimension greater than the average crystallite size of the film. Moreover, the compositional anomalies observed elsewhere in the crystallite boundaries, seem to indicate that the latter hamper the establishment of pseudo-periodic composition variations. As a result, the pseudo-periodic composition variations can then only be observed in the largest crystallites, as illustrated by Figure 7f, 7g and 7h. In this case, one approaches the crystallization states of the bulk oxides (iron cobaltites or manganese aluminates, for example [12, 31]) in which the pseudo-periodic alternations of phases generated by the spinodal transformation have already been demonstrated. It, therefore, seems reasonable to say that the absence of pseudo-periodic variations of composition within the crystallites is mainly due to the smallness of their size.

It should now be recognized that the development of pseudo-periodic alternations, generally induced by the spinodal transformation, can be inhibited by the nano-structure of the material. To our best knowledge, this observation was not previously reported in the literature.

#### 4. Conclusions

Until now, the pseudo-periodic alternations of different composition spinel phases were demonstrated only in iron cobaltites pre-annealed at high temperatures ( $\approx 900$  °C). These oxides, therefore, consisted of crystallites of large sizes. The thin films studied by our group were, however, prepared by sputtering, not so far from room temperature. In these films, it was not possible to observe such a pseudo-periodic microstructure even for samples processed under conditions conducive to spinodal decomposition and whose multiphase nature was clearly demonstrated by X-ray diffraction or Raman spectroscopy. This failure was attributed to sample preparation method that failed to isolate individual crystallites.

In this work, we have developed a specific preparation method which has made it possible to obtain sections parallel to the film plane. In these sections, individual crystallites can be observed and studied by different electron microscopy techniques. For a sample previously treated at 600 °C for 96 h, it was possible to confirm its transformation by a germination-growth process, leading to oxide phases rich in iron or cobalt. The microscopic observations revealed, however, that the core of crystallites was richer in cobalt than the areas near the grain boundaries. The semi-quantitative evaluation of the chemical compositions of the formed phases also showed that the germination - growth mechanism was not completed. The compositions observed do not reach the maximum values indicated in the literature. For the sample treated at 600 °C for 24 h under conditions favourable to the establishment of a spinodal decomposition and for which X-ray diffraction and Raman spectroscopy characterizations confirm a two-phase state, the spatial organization of the phases is similar to that observed for the 96 h treated sample. In particular, iron enrichment occurs at the grain boundaries and their proximity. However, in the largest crystallites or along their axis of elongation, it is possible to demonstrate the alternation of a cobalt-rich phase and an iron-rich phase reminiscent of the classical characteristics of the spinodal transformation.

All these observations suggest that the small crystallite size inhibits the formation of pseudo-periodic spinel phases alternations. A crystallite size effect on the development of the spinodal transformation is therefore highlighted. To our best knowledge, such effect was not previously reported in the literature.

#### Acknowledgements

This work was supported by a Scholarship from the Ministry of Education and Training of the Socialist Republic of Vietnam.

#### References:

- 
- [1] S.G. Mohamed, C-J. Chen, C.K. Chen, S-F. Hu, R-S. Liu, ACS Appl. Mater. Interfaces, 2014, **6**, 22701-22708. *High-performance lithium-ion battery and symmetric supercapacitors based on FeCo<sub>2</sub>O<sub>4</sub> nanoflakes electrodes.*

- [2] S.G. Mohamed, S.Y. Atti, H.H. Hassan, *Microporous Mesoporous Mater.*, 2017, **251**, 26-33. *Spinel-structured  $\text{FeCo}_2\text{O}_4$  mesoporous nanosheets as efficient electrode for supercapacitor applications.*
- [3] Z. Yan, D.A. Keller, K.J. Rietwyk, H.N. Barad, K. Majhi, A. Ginsburg, A.Y. Anderson, A. Zaban, *Energy Technology*, 2016, **4**, 809-815. *Effect of spinel inversion on  $(\text{Co}_x\text{Fe}_{1-x})_3\text{O}_4$  all-oxide solar cell performance.*
- [4] R.N. Bhowmik, V. Vasanthi, A. Poddar, *J. Alloys Compd.*, 2013, **578**, 585-594. *Alloying of  $\text{Fe}_3\text{O}_4$  and  $\text{Co}_3\text{O}_4$  to develop  $\text{Co}_{3x}\text{Fe}_{3(1-x)}\text{O}_4$  ferrite with high magnetic squareness, tunable ferromagnetic parameters, and exchange bias.*
- [5] P. Saxena, D. Varshney, *J. Alloys Compd.* 2017, **705**, 320-326. *Effect of d-block element substitution on structural and dielectric properties on iron cobaltite.*
- [6] M.G.M. Miranda, E. Esteves-Rams, M.N. Baibich, *Phys. Rev. B*, 2003, **68**, 014434. *Phase separation in  $\text{Cu}_{90}\text{Co}_{10}$  high-magneto-resistance materials.*
- [7] M.G.M. Miranda, A.T. da Rosa, M.N. Baibich, E. Esteves-Rams, G. Martinez, *Phys. B. Condens. Matter.*, 2004, **354**, 88-91. *Nanoscale transformations and GMR in bulk non-equilibrium Cu-Co alloys.*
- [8] S.A. Nikitov, P. Tailhades, C.S. Tsai, *J. Magn. Magn. Mater.*, 2001, **236**, 320-330. *Spin waves in periodic magnetic structures - magnonic crystals.*
- [9] V. Gulyaev, S.A. Nikitov, L.V. Zhirovskii, A.A. Klimov, P. Tailhades, L. Presmanes, C. Bonningue, C.S. Tsai, S.L. Vysotskii, Y.A. Filimonov, *JETP Letters*, 2003, **77**, 567-570. *Ferromagnetic films with magnon bandgap periodic structures: magnon crystals.*
- [10] J. Robin, *Ann. Chim.*, 1955, **12**, 389-412. *Recherches sur la constitution et la stabilité de quelques solutions solides à base d'oxyde de cobalt.*
- [11] M. Takahashi, M.E. Fine, *J. Am. Ceram. Soc.*, 1970, **53**, 11, 633-634. *Coercive force of spinodally decomposed cobalt ferrite with excess cobalt.*
- [12] M. Takahashi, J. Guimaraes, M.E. Fine, *J. Am. Ceram. Soc.*, 1971, **54**, 291-295. *Spinodal Decomposition in the System  $\text{CoFe}_2\text{O}_4$ - $\text{Co}_3\text{O}_4$ .*
- [13] I.H. Jung, S.A. Deckerov, A.D. Pelton, H.M. Kim, Y.B. Kang, *Acta Mater.*, 2004, **5**, 2, 507-519. *Thermodynamic evaluation and modelling of the Fe-Co-O system.*
- [14] W.W. Zhang, M. Chen, *Calphad*, 2013, **41**, 76-88. *Thermodynamic modeling of the Co-Fe-O system.*
- [15] L. André, S. Abanades, L. Cassayre, *J. Solid State Chem.*, 2017, **253**, 6-14. *High-temperature thermochemical energy storage based on redox reactions using Co-Fe and Mn-Fe mixed metal oxides.*
- [16] J.W. Cahn, J.E. Hilliard, *J. Chem. Phys.*, 1958, **28**, 258. *Free energy of a nonuniform system. I- Interfacial free energy.*
- [17] J.W. Cahn, *Acta Metall.*, 1961, **9**, 9, 795-801. *On spinodal decomposition.*
- [18] R.J. Harrison, A. Putnis, *Surv. Geophys.*, 1999, **19**, 461-520. *The magnetic properties and crystal chemistry of oxide spinel solid solutions.*
- [19] S. Hirano, T. Yogo, K. Kikuta, E. Asai, K. Sugiyama, H. Yamamoto, *J. Am. Ceram. Soc.*, 1993, **76**, 7, 1788-1792. *Preparation and phase separation behaviour of  $(\text{Co,Fe})_3\text{O}_4$  films.*
- [20] H. Le Trong, A. Barnabé, L. Presmanes, P. Tailhades, *Solid State Sci.*, 2008, **10**, 5, 550-556. *Phase decomposition study in  $\text{Co}_x\text{Fe}_{3-x}\text{O}_4$  iron cobaltites: synthesis and structural characterization of the spinodal transformation.*
- [21] N. Debnath, T. Kawaguchi, W. Kumasaka, H. Das, K. Shinozaki, N. Sakamoto, H. Suzuki, N. Wakiya, *J. Magn. Magn. Mater.*, 2017, **432**, 391-395. *As-grown enhancement of spinodal decomposition in spinel cobalt ferrite thin films by Dynamic Aurora pulsed laser deposition.*
- [22] H. Le Trong, T.M.A Bui, L. Presmanes, A. Barnabé, I. Pasquet, C. Bonningue, P. Tailhades, *Thin Solid Films*, 2015, **589**, 292-297. *Preparation of iron cobaltite thin films by RF magnetron sputtering.*
- [23] T.M.A. Bui, H. Le Trong, L. Presmanes, A. Barnabé, P. Tailhades, *CrystEngComm.*, 2014, **16**, 3359-3365. *Thin films of  $\text{Co}_{1.7}\text{Fe}_{1.3}\text{O}_4$  prepared by radio frequency sputtering-the first step towards their spinodal decomposition.*
- [24] H.M. Rietveld, *J. Appl. Crystallogr.*, 1969, **2**, 65-71. *A profile refinement method for nuclear and magnetic structures.*
- [25] J. Rodríguez-Carvajal, *Phys. B Condens. Matter*, 1993, **192**, 55-69. *Recent advances in magnetic structure determination by neutron powder diffraction*
- [26] H. Shirai, Y. Morioka, I. Nakagawa, *J. Phys. Soc. Jpn.*, 1982, **51**, 592-597. *Infrared and Raman spectra and lattice vibrations of some oxide spinels.*
- [27] V. G Hadjiev, M. N. Iliev, I. V. Vergilov, *J. Phys. Chem.*, 1988, **21**, 199-201. *The Raman spectra of  $\text{Co}_3\text{O}_4$ .*
- [28] P. Chandramohan, M. P. Srinivasan, S. Velmurugan, S. V. Narashimhan, *J. Solid State Chem.*, 2011, **184**, 89-96. *Cation distribution and particle size effect on Raman spectrum of  $\text{CoFe}_2\text{O}_4$ .*
- [29] Z. Wang, R. T. Downs, V. Pischedda, R. Shetty, S. K. Saxena, C. S. Zha, Y. S. Zhao, D. Schiferl, A. Waskowska, *Phys Rev B*, 2003, **68**, 094101. *High-pressure x-ray diffraction and Raman spectroscopic studies of the tetragonal spinel  $\text{CoFe}_2\text{O}_4$ .*

- 
- [30] O. N. Shebanova, P. Lazor, J. Solid State Chem. 2003, **174**, 424-430. *Raman spectroscopic study of magnetite (FeFe<sub>2</sub>O<sub>4</sub>): a new assignment for the vibrational spectrum.*
- [31] S. V. Cherepanova, O. A. Bulavchenko, E.Yu. Gerasimov, S. V.Tsybulya, CrystEngComm, 2016, **18**, 3411-3421. *Low and high temperature oxidation of Mn<sub>1.5</sub>Al<sub>1.5</sub>O<sub>4</sub> in relation to decomposition mechanism and microstructure.*

## Figure Caption list

**Figure 1:** Calculated phase diagram of the Co-Fe-O system in air according to thermodynamic models of I.H. Jung et al. [13] (black line) and W.W. Zhang [14] (red line). Dashed blue line represents the composition  $\text{Co}_{1.7}\text{Fe}_{1.3}\text{O}_4$  of the films studied in the present work. Dashed black bold lines represent the limit of the estimated coherent spinodal domain according to M. Takahasi [12].

**Figure 2:** a) XRD patterns of as-deposited  $\text{Co}_{1.7}\text{Fe}_{1.3}\text{O}_4$  film and annealed ones at 600 °C under air for various durations. b) Refined cubic lattice parameter of different spinel phases obtained after various annealing time at 600 °C. The value reported at zero corresponds to the as-deposited film. Black lines correspond to the limit of the miscibility gap. Dashed black lines represent the limit of the estimated coherent spinodal domain according to M. Takahashi [12].

**Figure 3:** a) Raman spectra of as-deposited  $\text{Co}_{1.7}\text{Fe}_{1.3}\text{O}_4$  film and annealed ones at 600 °C under air for 12, 24 and 96 h. Iron rich  $\text{Co}_{1.1}\text{Fe}_{1.8}\text{O}_4$  ( $x = 0.37$ ) and cobalt rich  $\text{Co}_{2.7}\text{Fe}_{0.3}\text{O}_4$  ( $x = 0.90$ ) powder samples are reported for comparison. b) Comparison of the calculated spectrum from weighted sum of  $x = 0.37$  and  $x = 0.90$  powder spectra (dot blue) with the one of 96 h annealed  $\text{Co}_{1.7}\text{Fe}_{1.3}\text{O}_4$  film (black line).

**Figure 4:** a) EDS maps obtained using iron (red) and cobalt (green)  $K\alpha$  and b) corresponding cross section STEM micrographs of the  $\text{Co}_{1.7}\text{Fe}_{1.3}\text{O}_4$  films annealed at 600 °C for 96 h. Local EDS analyses in iron-rich and cobalt-rich area are highlighted in spectra c). Atomic composition along the horizontal axis of area 3 is plotted in d).

**Figure 5:** Secondary electron and ionic SEM images showing the different stages of producing a plan view TEM specimen of the  $\text{Co}_{1.7}\text{Fe}_{1.3}\text{O}_4$  thin films (a) using FIB. First an area of film at the edge of the substrate is coated with Pt (b) and cross-section milled (c). Then the sample is removed from the chamber and re-mounted vertically (d). After a new lateral Pt coating (e), a trench is milled away from the back side (f) leaving a thick lamellar which is then lifted out in-situ (g, h). The sample is then attached to a copper support grid (i) and thinned ready for examination (j, k).

**Figure 6:** TEM analysis of the 96 h annealed  $\text{Co}_{1.7}\text{Fe}_{1.3}\text{O}_4$  thin film with a) in-plane STEM views and EDS mapping using b) cobalt (green) and c) iron (red)  $\text{K}\alpha$  rays, d) STEM-HAADF and e) STEM-BF views, f) h) STEM-HAADF views and g) i) EDS analysis with the corresponding compositions in at%.

**Figure 7:** TEM analysis of the 24 h annealed  $\text{Co}_{1.7}\text{Fe}_{1.3}\text{O}_4$  thin film with a) in-plane STEM views and EDS mapping using b) cobalt (green) and c) iron (red)  $\text{K}\alpha$  rays, d) HAADF STEM image and e) corresponding FFT-pattern, f) BF-STEM view and g) h) EDS analysis with the corresponding compositions in at%.

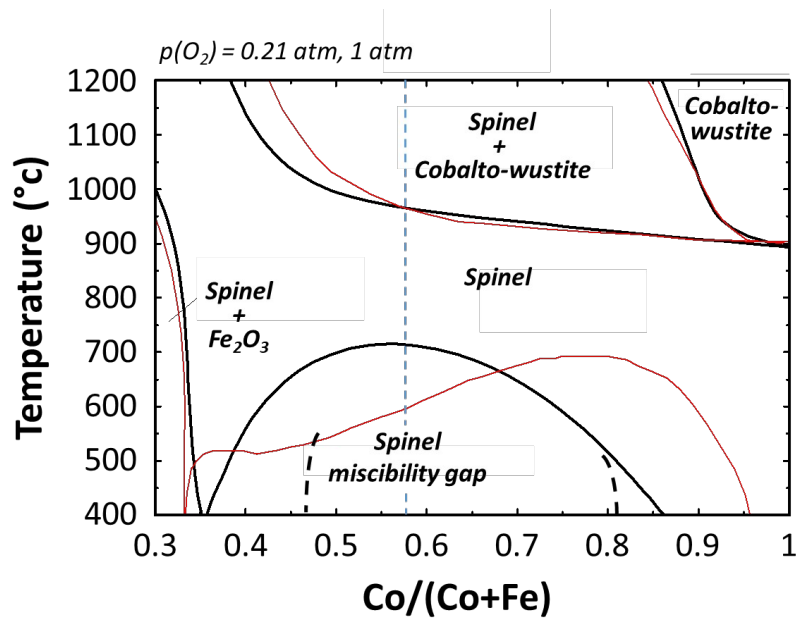


**Figure 1:** Calculated phase diagram of the Co-Fe-O system in air according to thermodynamic models of I.H. Jung et al. [13] (black line) and W.W. Zhang [14] (red line). Dashed blue line represents the composition  $Co_{1.7}Fe_{1.3}O_4$  of the films studied in the present work. Dashed black bold lines represent the limit of the estimated coherent spinodal domain according to M. Takahasi [12].

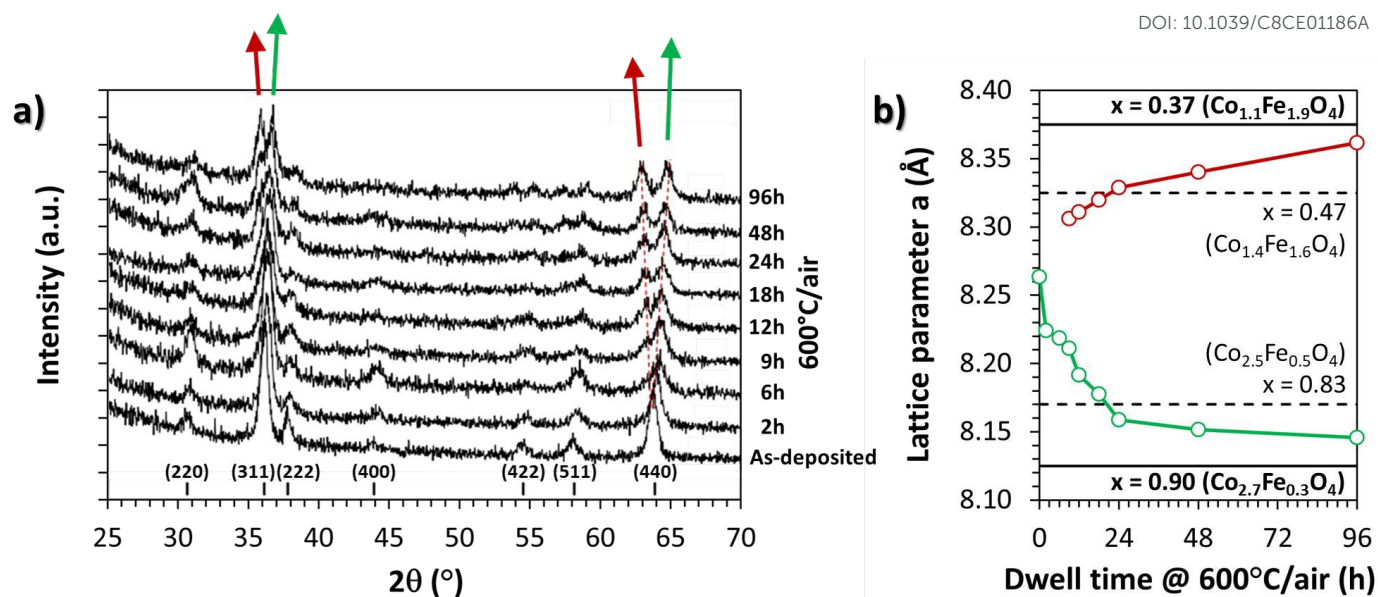


**Figure 2:** a) XRD patterns of as-deposited  $\text{Co}_{1.7}\text{Fe}_{1.3}\text{O}_4$  film and annealed ones at  $600^\circ\text{C}$  under air for various durations. b) Refined cubic lattice parameter of different spinel phases obtained after various annealing times at  $600^\circ\text{C}$ . The value reported at zero corresponds to the as-deposited film. Black lines correspond to the limit of the miscibility gap. Dashed black lines represent the limit of the estimated coherent spinodal domain according to M. Takahashi [12].

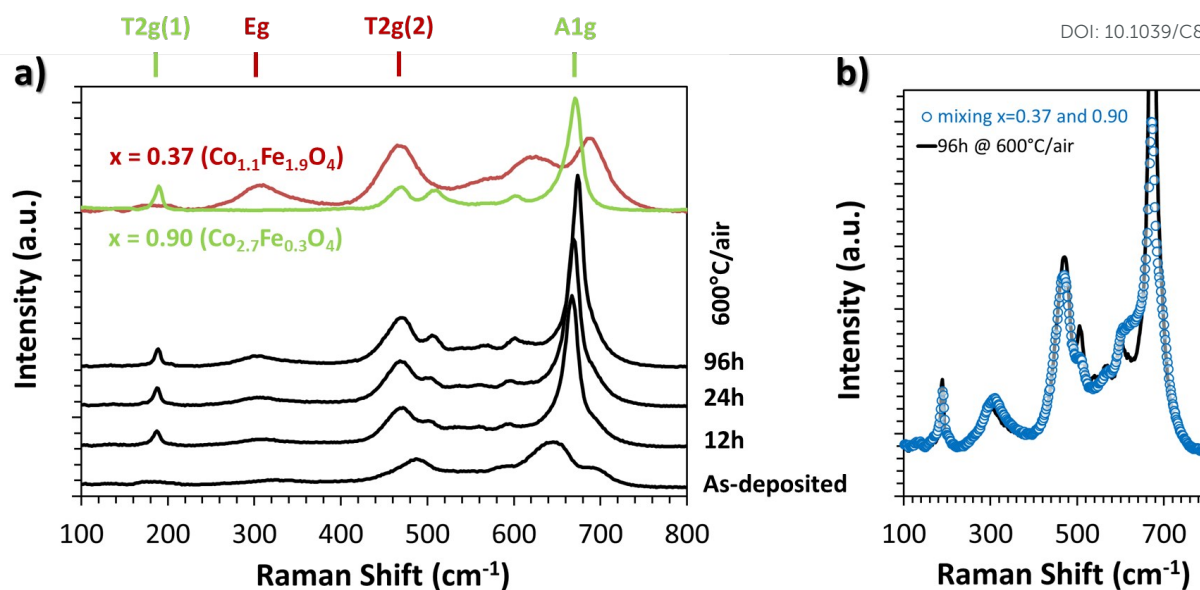


**Figure 3:** a) Raman spectra of as-deposited  $\text{Co}_{1.7}\text{Fe}_{1.3}\text{O}_4$  film and annealed ones at 600 °C under air for 12, 24 and 96 h. Iron rich  $\text{Co}_{1.1}\text{Fe}_{1.9}\text{O}_4$  ( $x = 0.37$ ) and cobalt rich  $\text{Co}_{2.7}\text{Fe}_{0.3}\text{O}_4$  ( $x = 0.90$ ) powder samples are reported for comparison. b) Comparison of the calculated spectrum from weighted sum of  $x = 0.37$  and  $x = 0.90$  powder spectra (dot blue) with the one of 96 h annealed  $\text{Co}_{1.7}\text{Fe}_{1.3}\text{O}_4$  film (black line).

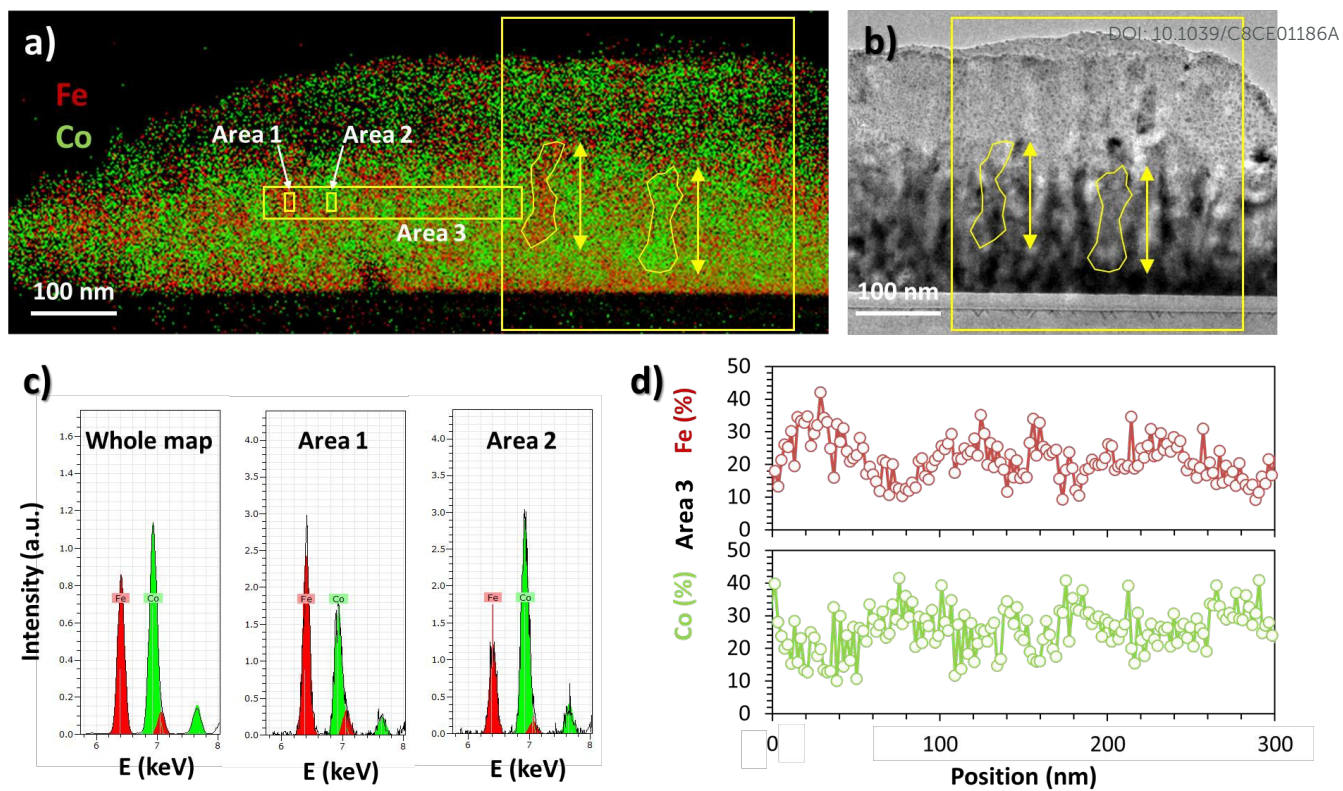


**Figure 4:** a) EDS maps obtained using iron (red) and cobalt (green)  $K\alpha$  and b) corresponding cross section STEM micrographs of the  $\text{Co}_{1.7}\text{Fe}_{1.3}\text{O}_4$  films annealed at 600 °C for 96 h. Local EDS analyses in iron-rich and cobalt-rich area are highlighted in spectra c). Atomic composition along the horizontal axis of area 3 is plotted in d).

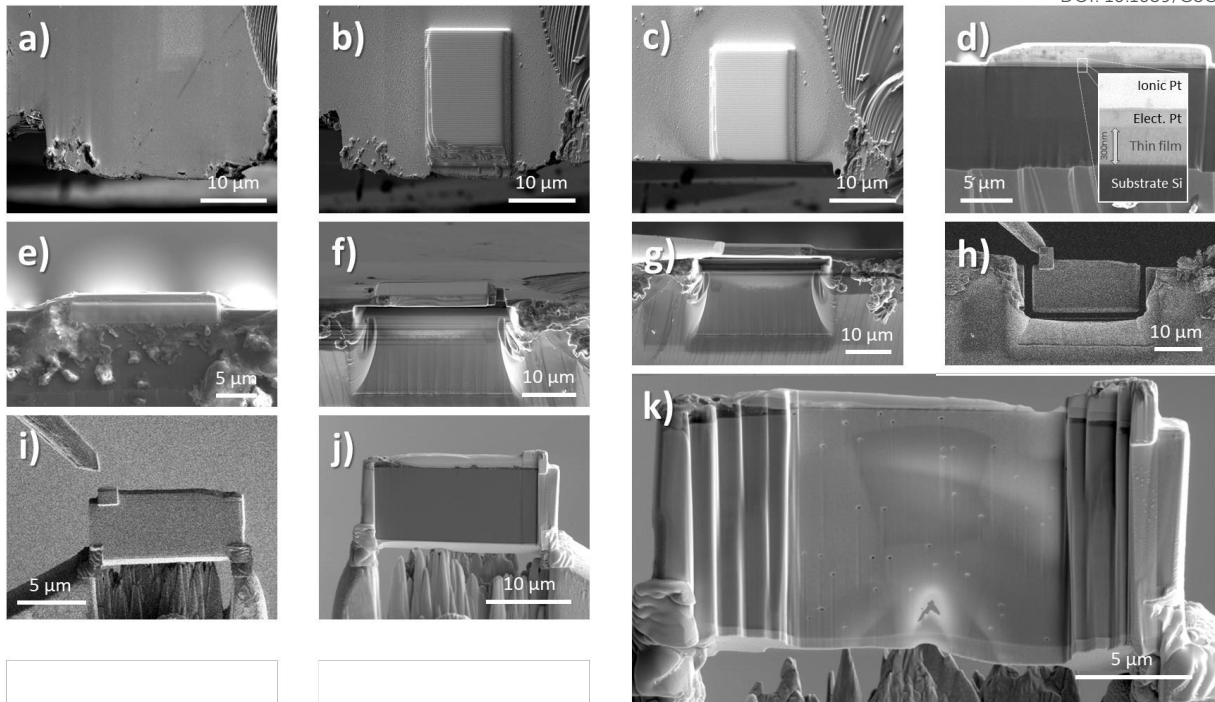


**Figure 5:** Secondary electron and ionic SEM images showing the different stages of producing a plan view TEM specimen of the  $\text{Co}_{1.7}\text{Fe}_{1.3}\text{O}_4$  thin films (a) using FIB. First an area of film at the edge of the substrate is coated with Pt (b) and cross-section milled (c). Then the sample is removed from the chamber and re-mounted vertically (d). After a new lateral Pt coating (e), a trench is milled away from the back side (f) leaving a thick lamellar which is then lifted out in-situ (g, h). The sample is then attached to a copper support grid (i) and thinned ready for examination (j, k).

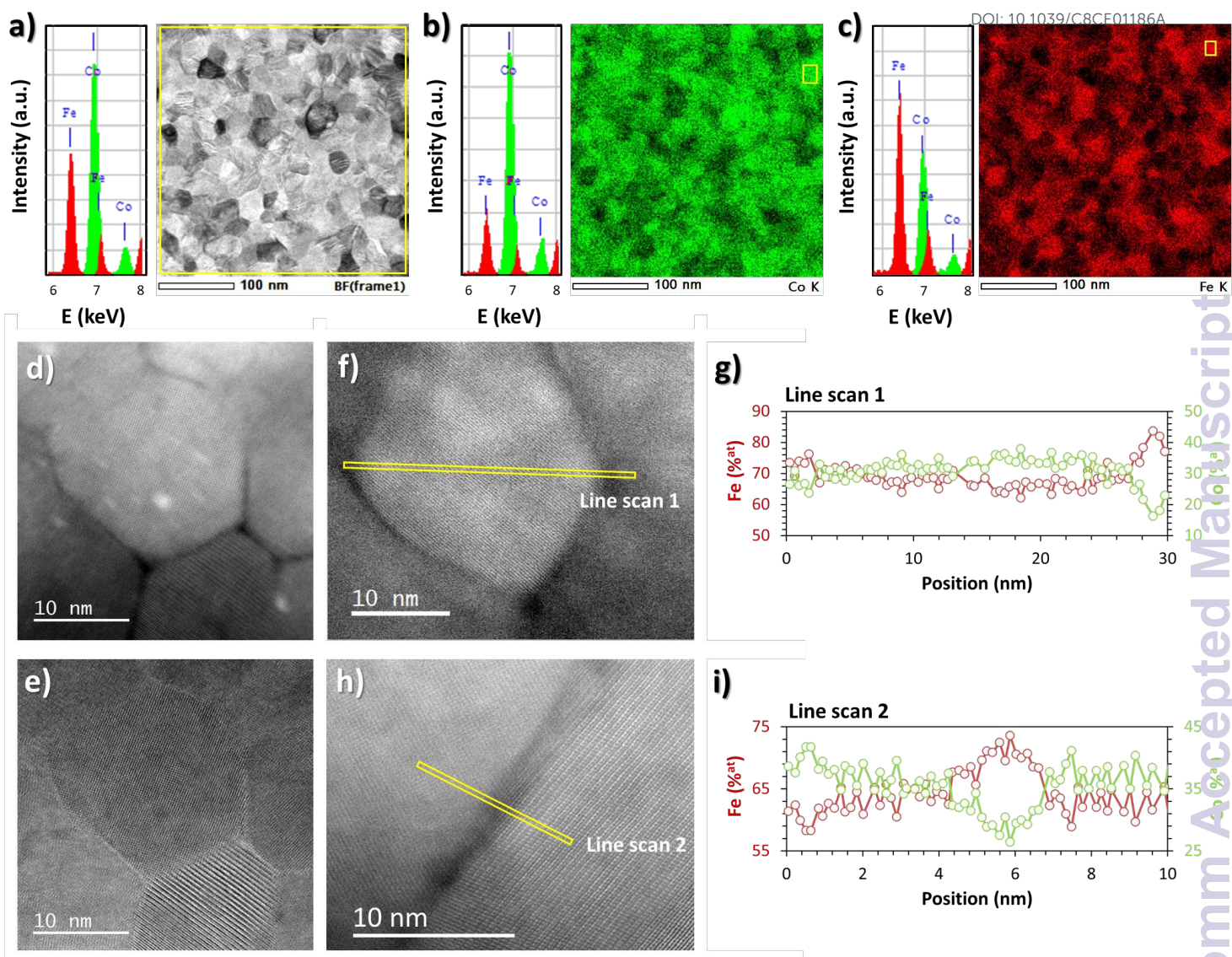


**Figure 6:** TEM analysis of the 96 h annealed  $\text{Co}_{1.7}\text{Fe}_{1.3}\text{O}_4$  thin film with a) in-plane STEM views and EDS mapping using b) cobalt (green) and c) iron (red)  $\text{K}\alpha$  rays, d) STEM-HAADF and e) STEM-BF views, f) h) STEM-HAADF views and g) i) EDS analysis with the corresponding compositions in at%.

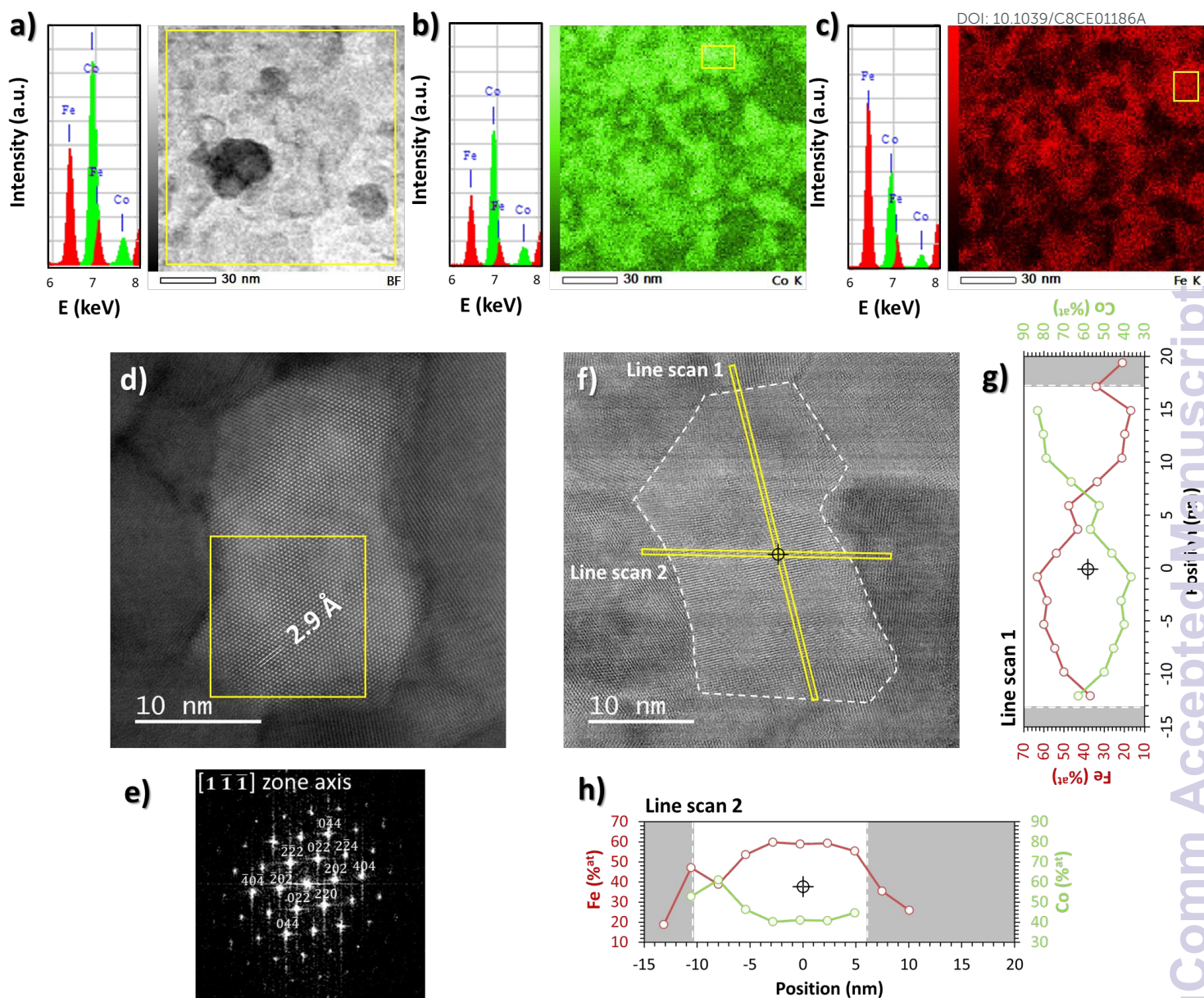


**Figure 7:** TEM analysis of the 24 h annealed  $\text{Co}_{1.7}\text{Fe}_{1.3}\text{O}_4$  thin film with a) in-plane STEM views and EDS mapping using b) cobalt (green) and c) iron (red)  $\text{K}\alpha$  rays, d) HAADF STEM image and e) corresponding FFT-pattern, f) BF-STEM view and g) h) EDS analysis with the corresponding compositions in at%.